

www.acsami.org Research Article

Electrochemical Sodiation Mechanism in Magnetite Nanoparticle-Based Anodes: Understanding of Nanoionics-Based Sodium Ion Storage Behavior of Fe₃O₄

Mohammad A. Islam,* Jared Bouldin, Junghoon Yang, and Sang-Don Han*



Cite This: ACS Appl. Mater. Interfaces 2022, 14, 50773-50782



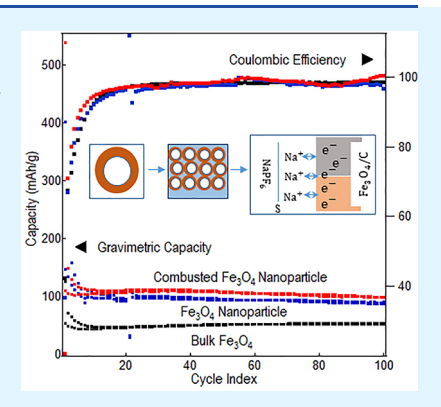
ACCESS I

Metrics & More

Article Recommendations

s Supporting Information

ABSTRACT: Electrochemical ion storage behaviors of Fe_3O_4 nanoparticles, as a representative transition metal oxide for an environmentally benign and low-cost anode for a sodium-ion battery, are thoroughly investigated through a combination of electrochemical analysis and diagnostics of Fe_3O_4 electrode cells, X-ray-based and spectroscopic analysis of material structure evolution as functions of depth of discharge (DoD) and state of charge (SoC), and first principle modeling. The gravimetric capacity is found to be 50 mA h/g for bulk Fe_3O_4 (50 nm average crystallite size) and 100 mA h/g—about a tenth of the theoretical prediction for complete conversion—for Fe_3O_4 nanoparticles (8.7 nm average particle size), respectively. A fundamental and mechanistic study of material evolution as functions of DoD and SoC shows that Fe_3O_4 does not allow electrochemical incorporation of Na^+ ions into the empty cation positions of the inverse spinel structure, leading to our assertion that electrochemical intercalation of Na^+ ions to conversion of the Fe_3O_4 anode in sodium-ion batteries is nonviable. A density functional



theory investigation points to the impracticality of the intercalation of Na^+ ions into Fe_3O_4 and further validates our experimental findings. We propose several possible mechanisms corresponding to the observed low capacity, including formation of solid electrolyte interphases with unfavorable properties and adsorption of Na^+ ions onto surfaces of nanoparticles and/or at heterointerfaces in Fe_3O_4 composite electrodes in a $NaPF_6$ -based electrolyte system.

KEYWORDS: ion storage behaviors, magnetite nanoparticle, sodium-ion batteries, nanointerfaces, nanoionics

INTRODUCTION

While lithium-ion batteries (LIBs) have been powering the technology of the 21st century, they face significant headwinds due to high cost, limited sourcing of critical materials, and carcinogenic compounds in their electrodes. Leveraging the large repertoire of knowledge on LIBs, therefore, research on sodium-ion batteries (SIBs) has begun in earnest based on several advantages: sodium is the second lightest alkali next to lithium; its electron affinity is almost identical to that of Li; and the standard reduction potential of Na/Na⁺ is only 0.34 V higher than that of Li/Li⁺. Add to these facts that sodium is essentially cheap and limitless on the earth and environmentally friendly, and the advantages of SIBs over LIBs for large-scale electrochemical energy storage systems are clear. ^{1–3}

For high-performance SIBs, the development of novel anode materials is essential. The main choice of anode for rechargeable batteries has been carbon allotropes. While graphitic carbon has been found to work well for Li $^+$ ion (de)insertion, the larger size of Na $^+$ ions prevents their intercalation into the 2D structure of graphite. The current state-of-the-art anode in SIBs is hard carbon (HC). HC, however, presents significant obstacles, including an expensive fabrication process requiring high temperatures, low initial Coulombic efficiency, a relatively low reversible capacity of \sim 370 mA h/g, and limited reversibility.

Transition metal oxides (TMOs) with the inverse spinel (IS) structure are being studied as an alternative anode for SIBs. The IS-TMO anodes undergo a complete conversion reaction—as opposed to the (de)intercalation processes of the layered electrodes. The conversion reactions are, in principle, multielectron processes, which gives IS-TMO anodes a clear advantage over the intercalation electrodes. Conversion-type anodes involve the following general reaction scheme: ⁵⁻¹⁵

$$M_aX_b + (bn)A \leftrightarrow aM + bA_nX$$

(e.g., $Fe_3O_4 + 8Na \leftrightarrow 3Fe + 4Na_2O$ for SIBs) (1)

where M = transition metal, X = anion, n = formal oxidation state of X, and A = Li or Na.

Full utilization of the electrode can be accomplished by nanostructuring to facilitate electrolyte penetration and

Received: July 20, 2022 Accepted: October 19, 2022 Published: November 1, 2022





electron/ion diffusion. The potentials for high capacity and reversibility in conversion-type batteries with nanostructured anodes lie in the large number of electrons exchanged per mole of the electrode material and the formation of metal nanoparticles (NPs) in the discharge half cycle, respectively. As seen in the equation above, eight electrons are transferred per mole of the anode in each half cycle, resulting in an anode capacity of 926 mA h/g. Additionally, the metal NPs (e.g., 3Fe, eq 1) formed at discharge possess large surface energy which favors the reverse reaction when voltage is applied for recharging. Thus, the tendency of the electrodes to avoid a large penalty in surface energy of metal NPs and the large number of electrons transferred in each cycle are keys for high utilization of IS-TMO nanostructured electrodes.

Investigation of IS-TMOs as a rechargeable battery anode started in earnest with the seminal paper of Thackeray et al. that proposed an intercalation to conversion model of Fe_3O_4 anodes in LIBs. This model depends on the robustness of the IS structure of the Fe_3O_4 system that permits additional cation placements in the octahedral and tetrahedral positions of the unit cell (Figure S1). ¹²

Thackeray et al. argued that, upon initial lithiation, the 8a $\mathrm{Fe^{3+}}$ ions are reduced and displaced to the neighboring empty octahedral 16c sites, and that upon further lithiation, the $[\mathrm{Fe^{2+}}]_{16\mathrm{d}}\mathrm{O_4}$ subarray remains unchanged and acts as a robust close-packed-anion 3D framework: 12

$$(Fe^{3+})_{8a}(Fe^{3+/2+})_{16d}O_4 \xrightarrow{x_c Li} (Li_{x_c}^+ Fe^{3+/2+})_{16c}(Fe^{3+/2+})_{16d}O_4$$
 (2)

Beyond a certain fraction of Li per formula unit of Fe₃O₄, the insertion process becomes nonviable; a breakage of the original crystal system occurs, and conversion takes place.

In addition to the attractiveness of the intercalation to conversion model of eq 2, Fe $_3O_4$ itself is an attractive anode material. It is cheap, possesses a conductivity of σ = $2\times10^4\, \rm Sm^{-1}$ (just an order shy of metallic conductivity), and leaves an almost nonexistent environmental footprint. Thus, the Thackeray model engendered significant research on Fe $_3O_4$ as a viable anode for LIBs and SIBs. $^{13-15}$

He et al. and Zhang et al. performed exhaustive studies of the Thackeray model on lithiation of ${\rm Fe_3O_4}$ nanomaterials. 13,14 Through *ex situ* and *in situ* experimental techniques, they demonstrated the validity of the model proposed by eq 2 in the first cycle. The reversible capacity was, however, close to two electron equivalents or ~200 mA h/g. Similar efforts in demonstrating that the model of eq 2 works for SIBs have, however, shown mixed success. While many of these studies started out with the Thackeray model as the motivation of their research, they ended up focusing on improving electrochemical performance by optimizing the extraneous features of materials and the process conditions. $^{9-11}$ As we show later in the Results and Discussion section, Komaba et al.'s assertion that ${\rm Na^+}$ ions are inserted into the ${\rm Fe_3O_4}$ inverse spinel crystal structure is contradicted by their own data. 9

Our research is thus motivated by the lack of mechanistic understanding of conversion-type electrochemistry in Fe_3O_4 as an anode in SIBs. We focus on the fact that the commonly accepted notion that the science developed for LIBs can be applicable to SIBs has been disproved but has continued to be practiced. We investigated Na^+ ion storage behaviors in bulk and NP forms of Fe_3O_4 . While our gravimetric capacity for the anode was commensurate with what other research groups have observed, it is still about one tenth of the theoretical capacity.

For a molecular-level understanding of electrochemical Na⁺ ion storage in Fe₃O₄ as functions of depth of discharge (DoD) and state of charge (SoC), electrochemical analysis, post-mortem Xray-based and spectroscopic characterization, and X-ray emission spectroscopy were employed. These studies reveal that the intercalation to conversion mechanism proposed by eq 2 is unworkable for Na⁺ ions in Fe₃O₄. In addition, our attempts at performing a density functional theory calculation of the stability of the Na_xFe₃O₄ system (eq 2) yielded unphysical results, pointing to the inability of the Fe₃O₄ system to accommodate Na+ ions. Finally, we provide several possible explanations for the observed electrochemical behaviors of the Fe₃O₄ anode in SIBs based on a combination of solid electrolyte interphase formation/evolution, surface chemistry of NPs, and ionic storage and conductivity enhancement at nanointerfaces (nanoionics).

EXPERIMENTAL SECTION

Material Synthesis and Characterization. Monodisperse magnetite Fe₃O₄ NPs were synthesized via reductive decomposition of Fe-precursors in a high-boiling-point organic solvent as described in ref 17. For some studies, the inert surfactants were removed by annealing the NPs in an oven at 300 °C in the ambient for 1 h. The size and the crystallinity of the Fe₃O₄ NPs were characterized using an FEI F20 transmission electron microscope (TEM) and Bruker Instruments X-ray diffractometer (XRD). The morphology of the electrode slurry was investigated with a TESCAN MIRA field emission scanning electron microscope (FESEM). Sodiation of Fe₃O₄ NP-based electrodes as functions of DoD and SoC was qualitatively studied through energy dispersive spectroscopy (EDS)-assisted elemental mapping, utilizing the same TESCAN MIRA FESEM system. To determine the inherent electrochemical properties of Fe₃O₄, bulk Fe₃O₄ [iron (II, III) oxide] was procured from Sigma-Aldrich [nanopowder, 50-100 nm particle size (SEM), 97% trace metals basis].

Electrode and Cell Fabrication. Slurries were made with 70 wt % Fe₃O₄ NP active materials, 20 wt % carbon black (C45, TIMCAL), and 10 wt % polyvinylidene fluoride (PVdF, Solvay) binder. 2-3 mL of Nmethyl-2-pyrrolidone (NMP, Sigma-Aldrich) was added, and the mixture was mixed in a slurry mixer. Films of the slurry were fabricated by tape casting on a carbon-coated copper current collector. Electrochemical coin-type cells were fabricated using these Fe₃O₄ slurry films as the working electrodes and punched sodium foil disks as the counter/reference electrodes. Typical mass loading of the active material Fe₃O₄ NPs on the electrode (15.5 mm diameter) was in the range 1.5-2.5 mg. 1 M sodium hexafluorophosphate (NaPF₆, Sigma-Aldrich) in 50:50 vol % of ethylene carbonate (EC, Tomiyama Pure Chemical Industries) and propylene carbonate (PC, Tomiyama Pure Chemical Industries) with a water content of <30 ppm was used as an electrolyte. A Whatmann GF/F glass fiber was used as a separator. For comparison, similar studies on the Fe₃O₄ slurry films were performed using Li-ion half-cells with a 1.0 M lithium hexafluorophosphate (LiPF₆, Sigma-Aldrich) in a 50:50 vol % mixture of EC and diethyl carbonate (DEC, Sigma-Aldrich) electrolyte and a Celgard 2400 polypropylene separator.

Electrochemical Analysis and Diagnostics. The cells were cycled galvanostatically at a rate of approximately C/20, which was 50 mA/g for the conversion reaction of Fe_3O_4 with Na^+ ions (eq 1). Most cells were cycled for 100 cycles. The primary focus of this research was, however, to determine the crystal structure evolution of Fe_3O_4 as functions of DoD and SoC. Accordingly, a series of cells were fabricated with electrodes based on Fe_3O_4 NPs annealed to remove surfactants prior to slurry formation and subjected to fractional galvanostatic discharge/charge cycles. The voltage vs specific capacity profiles of these cells labeled A–H considering their discharge and charge states (vs Na/Na^+) are shown in Figure S2. Upon arrival at the desired DoD and SoC, the cells were removed from the testing station. Each cell was then disassembled and the electrode retrieved. Following this, the

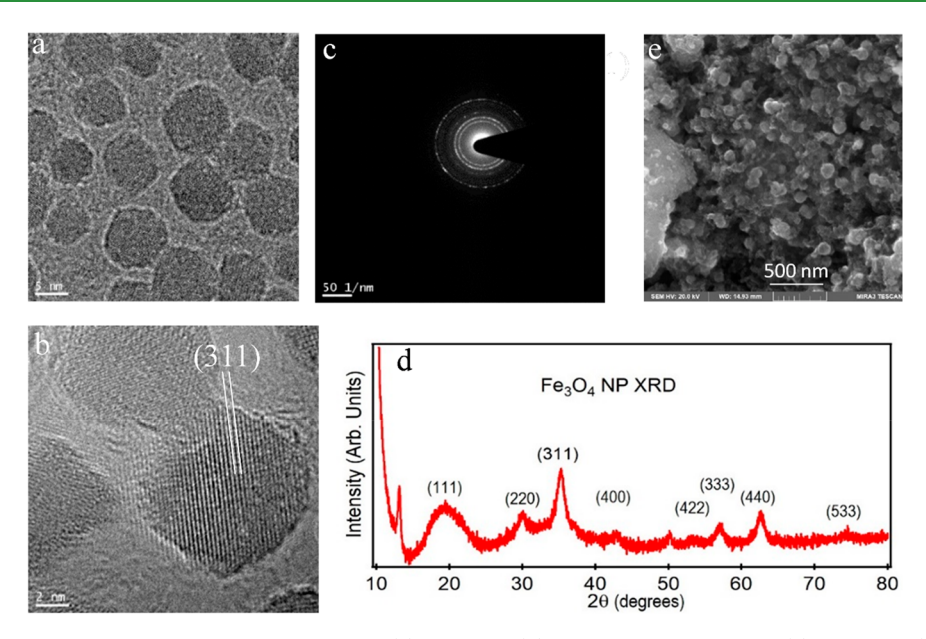


Figure 1. Synthesized Fe₃O₄ NPs were characterized using TEM (a), HRTEM (b), selective area diffraction (c), and XRD (d). (e) FE-SEM images taken from the pristine electrodes show good mixing of the different components of the electrode slurry. The scale bars in panels a, b, and e are 5, 2, and 500 nm, respectively.

electrodes were gently cleaned by using dimethyl carbonate (DMC, Sigma-Aldrich) for further characterization.

Advanced Characterizations. XRD patterns and Raman scattering spectra were collected from the Fe₃O₄ NP anodes as functions of DoD and SoC (samples A-H in Figure S2). Raman spectra were excited using the linearly polarized output of a solid state laser (785 nm) with 7 mW of power in a spot diameter of \sim 1.0 μ m at the sample and were dispersed and detected using a single-axis monochromator equipped with a charge-coupled detector array (Horiba XploRA, Edison, NJ). All Raman spectra were collected unpolarized and in the backscattering geometry.

X-ray emission spectroscopy (XES) studies were carried out on the cycled anodes (samples A-H) to determine the occupation of Fe²⁺ and Fe3+ in Fe3O4 and the possible reaction pathway from the initial intercalation of Na⁺ ions into the inverse spinel structure of Fe₃O₄ to the eventual conversion to metal NPs and sodium oxides (eq 1). Specifically, the cation configurations in Fe₃O₄ and Na_xFe₃O₄ were characterized using XES for reliable information on cation oxidation states. This was accomplished by a site selective XES analysis by taking advantage of the spin, oxidation state, and ligand-sensitive $K\beta_{1,3} + K\beta_{2,5}$ spectra. The XES spectra were collected using five spherically bent analyzer crystals [Si(533) for Fe K β] arranged in a Rowland geometry and detected using a Pilatus 100K area detector. The energy of the incident X-ray beam was tuned by means of a Si(111) double-crystal monochromator and was set to 9 keV. The beam size used was 100 \times 100 µm. A Rh-coated mirror was used for harmonic rejection. To minimize the attenuation of the fluorescent radiation, the area between the spherical analyzers, detector, and sample was filled with helium gas. The emission spectra were collected with a step size of 0.30 eV. For all samples, up to five scans each were carried out at fixed position on the sample and were averaged to obtain the final spectra for the sample.

Density Functional Theory (DFT)-Based Calculations. DFT calculations were performed using Quantum Espresso software, which utilizes a plane wave basis set in the expansion of the Kohn-Sham single particle wave functions. The ion-electron interactions were approximated using the projector augmented wave (PAW) potentials. Both the kinetic energy cutoff and Γ -centered Monkhorst-Pack kpoint grid were tested for convergence against a 1 meV/atom threshold. It was determined that a 700 eV kinetic energy cutoff and a $12 \times 12 \times$ $12/1 \times 1 \times 1$ k-point grid for the unit cell were sufficient. All structural relaxations and energy calculations were performed using the conjugate-gradient algorithm, and the ground state configuration was considered reached upon net forces on atoms falling below 0.01 eV/Å. Visualization for Electronic and Structural Analysis (VESTA) software was used to build the crystal structures.

RESULTS AND DISCUSSION

Materials. Electrochemical sodiation was carried out on bulk Fe₃O₄ (average crystallite size 50 nm) and Fe₃O₄ NPs. The average diameter of the as-synthesized Fe₃O₄ NPs was approximately 8.93 nm, as determined by averaging based on several TEM images (Figure 1a). A high-resolution TEM (HRTEM) image (Figure 1b) and selected area diffraction patterns (Figure 1c) demonstrate that the Fe₃O₄ NPs are crystalline, and the lattice fringes are indexed to the (311) planes. XRD (Figure 1d) and the accompanied crystal plane designations show that the as-synthesized Fe₃O₄ NPs crystallize in the inverse spinel structure. Using the most intense peak at 2θ = 35.262° , we determined a lattice constant of 8.564 Å, which is very similar to what is available in the literature. 9-12 In addition, an average crystallite size of 8.72 nm was determined using the Scherrer equation with the fwhm of the (311) peak, which is close to the value based on TEM measurements. FESEM images (Figure 1e) taken from the electrodes show that the carbon flakes are well mixed with the NPs on copper substrates.

Electrochemical Analysis. The theoretical capacity of the conversion-type Fe₃O₄ anode is 926 mA h/g in SIBs (and LIBs), as determined from eq 1, compared with the practical capacity of around 327 mA h/g for hard carbon. Li half-cells with Fe₃O₄ NP electrodes were tested first to ensure whether our Fe₃O₄ NPs are well synthesized and electrochemically active. As shown in Figure S3, the synthesized Fe₃O₄ NP-based anode in Li half-cells demonstrates an initial capacity of around 1250 mA h/g and subsequent reversible capacity of over 500 mA h/g; these capacities are on par with or larger than what was observed in recent articles. 13,14 In addition to the galvanostatic discharge/ charge cycling, the electrochemical behaviors of the Fe₃O₄ NPbased anodes in Li-ion half cells were analyzed using a corresponding differential capacity (dQ/dV) plot (Figure S3c). We note that the first cycle discharge curve in the voltage

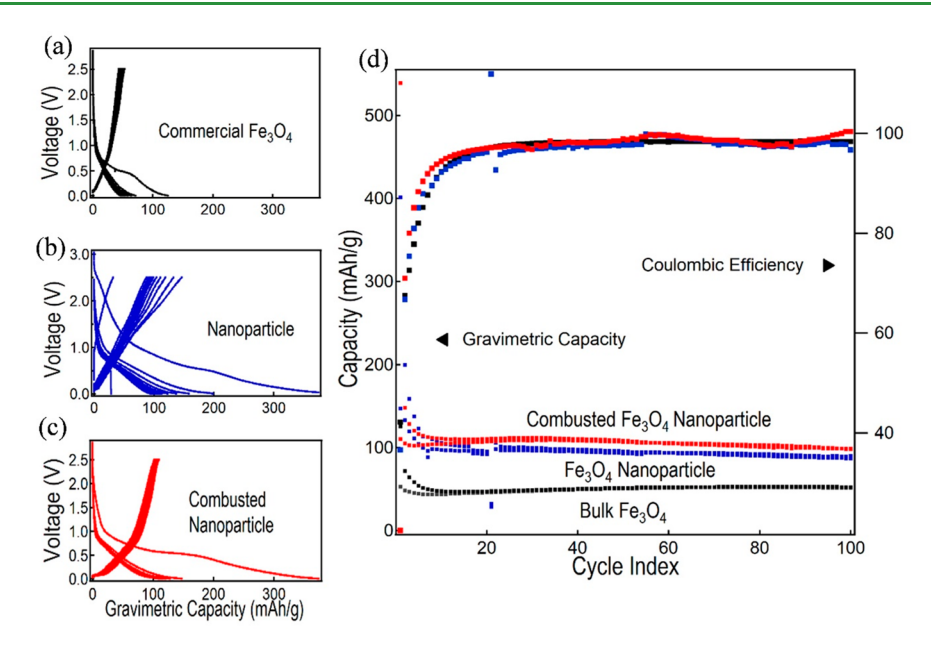


Figure 2. Voltage vs gravimetric capacity profiles of bulk Fe_3O_4 (a), synthesized Fe_3O_4 NP- (b), and combusted Fe_3O_4 NP-based anodes (c). (d) Cycling performance of those electrodes.

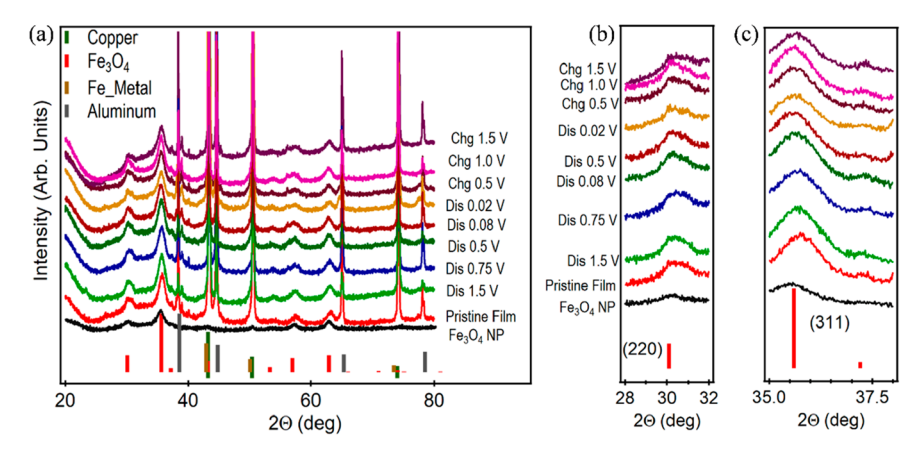


Figure 3. (a) XRD patterns of the Fe_3O_4 NP anodes as functions of DoD and SoC, along with that of the Fe_3O_4 NPs and of the pristine electrode. A comparison of the cycled electrodes with the original NPs shows no discernible changes as the electrodes undergo systematic discharging and charging. Closer looks at the diffraction peaks corresponding to the reflection from the (220) (b) and (311) (c) crystal planes show negligible changes. The color designations for panel c vis-à-vis DoD and SoC are identical to those of panel b.

vs gravimetric capacity profile (Figure S3a) clearly shows all of the sloping features and the plateaus that were seen in refs 13 and 14, which describe the systematic intercalation to conversion reactions of the Thackeray's model and confirm that our materials synthesis and battery fabrication methodology are all sound.

Na half-cells, cycled galvanostatically at a rate of approximately C/20, show much lower capacities for both bulk Fe_3O_4 -based electrodes and synthesized Fe_3O_4 NP-based electrodes compared with those of Li half-cells. The reversible capacity of the Na half-cells with bulk Fe_3O_4 -based anodes is around 54 mA h/g with an initial 160 mA h/g capacity, while the cells with Fe_3O_4 NP-based anodes show a reversible capacity of 94 mA h/g—almost a 100% increase compared to bulk—with an initial 401 mA h/g capacity as shown in Figure 2a,b,d. It is noteworthy that the reversible capacity is further improved by another 10% with an initial 539 mA h/g capacity when the Fe_3O_4 NPs are processed to remove the organic ligands from their surfaces, as shown in Figure 2c,d. The detailed electrochemical analysis of

the Fe_3O_4 NP-based anodes in Na-ion half cells based on a differential capacity (dQ/dV) plot is noted in the Supporting Information (Figure S4).

Before proceeding into the next part of the paper, we note here that this paper is not about improving the electrochemical performance of sodium-ion half-cells with Fe_3O_4 -based anodes. This has been done in previous studies, and our results either exceed or are competitive with the currently published results. For example, in ref 9, the first cycle discharge capacity is in the range of 150 mA h/g, and in ref 11, it is 643 mA h/g. In addition, composite active materials composed of Fe₃O₄ and a second complementary material like FeS, Fe2O3, graphene, carbon nanoparticle, and multi-heteroatom-dopants exhibits capacities in the range $169-350 \text{ mA h/g.}^{18-22}$ Other anode materials like MoS₂-reduced graphene oxides, NiS_{1.03} nanoparticles with Sdoped reduced graphene oxide, and 3D nanoflower-like V₃S₄ exhibit sodium storage capacities as high as 572 mA h/g at a 100 mA/g rate. 23-26 Our research is instead focused on providing a fundamental and mechanistic understanding of the ion storage

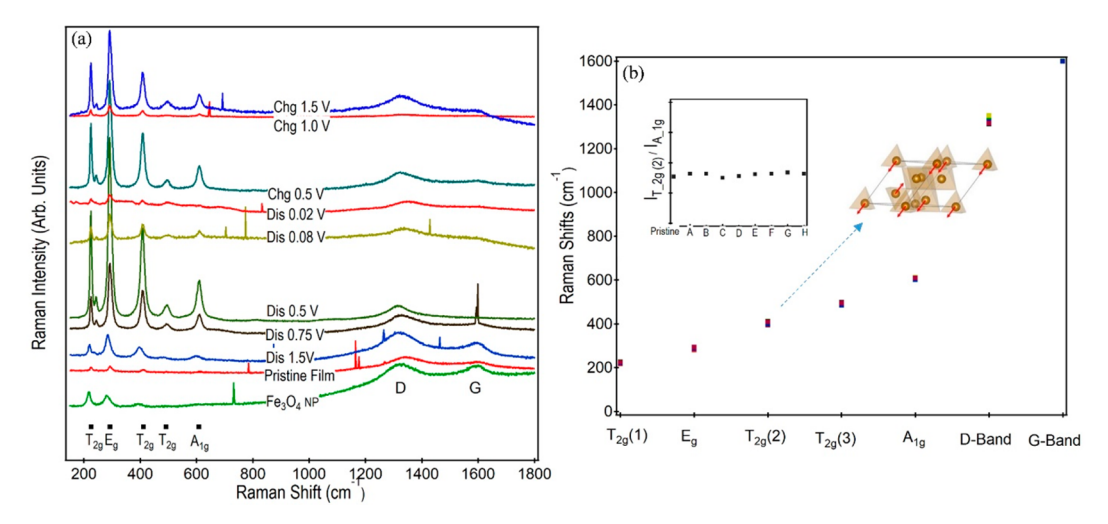


Figure 4. Raman spectra of Fe₃O₄ NP anodes as functions of DoD and SoC, along with that of the Fe₃O₄ NP-based slurry and of the pristine electrode as references. (a) Full range scans show the five Raman active modes as well as the G and D bands of carbon. All Raman spectra were peak-fitted to determine the peak locations. (b) Individual Raman modes as functions of DoD and SoC show negligible changes. The left inset of panel b shows a constant value for the ratio of the $T_{2g}(2)$ peak intensity that is responsible for the vibration of the 8a Fe³⁺ ions to the A_g intensity. The right inset shows the normal mode vibration of the T_{2g} (2) mode.

behaviors and possible failure mechanisms in single phase Fe₃O₄ as a conversion-type anode in SIBs.

Phase Transitions. Structural changes of the Fe₃O₄ anodes as functions DoD and SoC were investigated utilizing XRD and Raman spectroscopy. Based on the XRD patterns of pristine Fe₃O₄ NPs (Figure 1d), and of the pristine and cycled electrodes (Figure 3a), it is clear that the Fe₃O₄ NPs are crystallized in the inverse spinel structure. X-ray peaks corresponding to Cu metal and Fe and Al impurities present in the Cu current collector are also seen in Figure 3a. It is notable that there are negligible changes in the intensity and position of the Fe₃O₄ peaks as the electrodes are discharged and charged at different DoD and SoC, which is not too different from earlier experimental and simulation studies by Komaba et al. indicating that the (220) peak would weaken upon discharge if migration of Fe³⁺ ions from the tetrahedral 8a sites to the octahedral 16c sites were to take place. When they performed electrochemical insertion studies of Li⁺ ions into nanocrystalline Fe₃O₄, they found that the (220) reflection peak indeed weakened upon discharge and regained strength after charge, indicating the validity of the model proposed by eq 2. However, their electrochemical insertion studies of Na⁺ ions into nanocrystalline Fe₃O₄ show negligible changes in the (220) peak intensity and position, similar to our results in Figure 3b. For clarity, we also show the most intense peak (311) (Figure 3c), which also shows insignificant changes as functions of DoD and SoC. Therefore, it can be concluded that electrochemical insertion and deinsertion of Na⁺ ions into/from the inverse spinel structure of Fe₃O₄ could be unworkable, correlating the observed low capacity of the material (Figure 2).

Complementary Raman analyses were performed on the Fe₃O₄ NP-based slurry and electrodes as shown in Figure 4. Nanoscale unique properties in materials including quantum confinement, surface strain, and chemistry are extremely important for battery performance, and these can be studied extensively utilizing Raman spectroscopy. Due to the potential of Fe₃O₄ as a battery anode, a vast amount of literature on Raman studies of the material already exists. Specifically, Shebanova et al. showed that it is difficult to detect all five Raman active modes—symmetries of A_{1g} , E_{g} , T_{2g} , T_{2g} , and T_{2g} —

of Fe₃O₄, and the Raman modes across different studies vary significantly. For example, the difference in Raman peak positions of Fe₃O₄ was found to be as much as 30 cm⁻¹ when the exciting laser source was changed from 532 to 785 nm. 27,28 Therefore, the Raman spectra of synthesized Fe₃O₄ NPs in the slurry and in the electrodes with conductive carbons and binders were carefully assigned the following normal mode symmetries based on an extensive literature survey: T_{2g} (1) at 226.4 cm⁻¹, E_g at 292.8 cm⁻¹, T_{2g} (2) at 411.9 cm⁻¹, T_{2g} (3) at 492.4 cm⁻¹, and A_{1g} at 608.7 cm⁻¹, as shown in Figure 4a. In addition, characteristic Raman shifts known as the G and D bands from the conductive carbons in the electrode were also assigned. Then, Raman spectra were collected from the pristine and cycled electrodes at different DoD and SoC (samples A–H, Figure S2). The Raman spectrum of the pristine electrode is identical to that of the mixed slurry indicating that the electrode coating and drying steps may not affect the material's structure. More remarkable is that there are negligible changes in the Raman spectra from the subsequent samples. In Figure 4b, we plotted the individual modes as functions of DoD and SoC and see almost perfect overlap of all the Raman shifts of individual symmetries from each sample.

Normal mode enumeration shows that the Raman active modes of Fe₃O₄ result from collective motions of the Fe³⁺ ions located at the 8a Wyckoff positions (T_d symmetry) and the O atoms at the 32e Wyckoff positions (O_h symmetry). The Fe³⁺ and Fe²⁺ cations located at the 16c Wyckoff positions do not participate in Raman modes. Specifically, the 8a Fe³⁺ mode is T_{2g} (2) at 411.9 cm^{-1} . If the displacement of the Fe³⁺ ions from the 8a Wyckoff positions were to take place according to eq 2, gradual weakening of this Fe³⁺ mode intensity, compared to the other modes, could be observed. Furthermore, if the Fe³⁺ ions were to partially vacate the Raman active 8a positions, as prescribed in eq 2, we should observe changes to the existing mode frequency due to change in mode normal mass. The frequency Γ of a normal mode is inversely proportional to the square root of the reduced mass M_{Γ} of the atoms participating in the mode: $\Gamma \infty \sqrt{\frac{1}{M_{\rm r}}} = \sqrt{\sum \frac{1}{{\rm i} M_{\rm i}}}$. As shown in the right inset of

Figure 4b, only two tetrahedral Fe³⁺ ions participate in the $T_{2\sigma}$

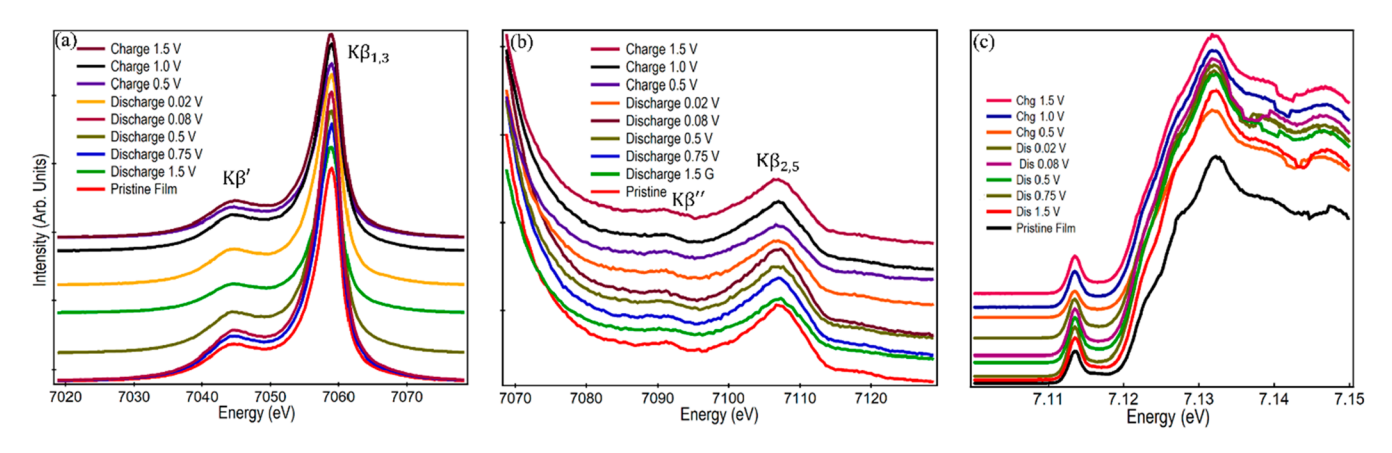


Figure 5. XES spectra of the Fe₃O₄ NP-based anodes as functions of DoD and SoC along with that of a pristine electrode as a reference. $K\beta_{1,3}$ and $K\beta'$ features (a) and $K\beta_{2,5}$ and $K\beta''$ features (b) show negligible change as functions of DoD and SoC. (c) Higher-resolution HERFD scans also show negligible changes.

(2) vibration, and as such, migration of a small fraction of these ions to the 16c position would change the frequency drastically. Furthermore, we have plotted the ratios of the T_{2g} (2) mode intensity to the A_{1g} mode intensity in the left inset of Figure 4b, and the ratios show an almost constant value. The facts that the frequency of the T_{2g} (2) modes does not change and that the intensity of the T_{2g} (2) mode with respect to the A_{1g} mode does not change as functions of DoD and SoC point to our assertion that Na⁺ ions may not be incorporated into the inverse spinel structure in Fe₃O₄, further pointing to the validity of our assertion based on the XRD studies (Figure 3).

Transition Metal Redox Chemistry. Following the observation of nonviability of Na⁺ ion insertion into the crystal structure of Fe₃O₄, we turned to more direct study to observe the redox couple Fe3+/Fe2+ in the Fe3O4 system by analyzing the cycled Fe₃O₄ anodes using X-ray emission spectroscopy (XES). XES studies commence with creating a core hole in transition metals (e.g., Fe) using X-ray beams. The core hole created after the ionization of an electron is unstable and decays rapidly via fluorescence (or Auger) processes. The fluorescence events following the photoabsorption of X-ray photons can be detected using XES. The most probable fluorescence event is a 2p electron refilling the 1s core hole, giving rise to a so-called K α emission line. Approximately 1 order of magnitude less likely is a 3p to 1s transition that creates a $K\beta$ emission line. For a transition metal with unpaired d electrons, the 3p-3d exchange coupling results in spectral splitting, giving rise to $K\beta_{1,3}$ and $K\beta'$ spectral features. Additionally, one can also observe the least probable event—a valence electron refilling the 1s core hole. This gives rise to valence-to-core (VtC) emission lines, $K\beta_{2,5}$ and $K\beta''$, which correspond to transitions from ligand np and ns orbitals to the metal 1s, respectively.^{29–31}

The relevance of XES studies to our investigation of Fe_3O_4 as the SIB anode is that Fe^{3+} and Fe^{2+} have different $K\beta_{1,3}$ and $K\beta'$ spectral features in principle, and Na^+ insertion into the crystal structure of Fe_3O_4 should change some of the Fe^{3+} to Fe^{2+} to satisfy charge neutrality. As a result, we should observe a systematic change of the XES features as functions of DoD and SoC

The resolution between the XES spectra of Fe²⁺ and Fe³⁺ is, however, more nuanced, due to the "accidental" coincidence of d orbital filling, covalency, and spin ordering in Fe. In general, the splitting between $K\beta_{1,3}$ and $K\beta'$ decreases, and the position of $K\beta_{1,3}$ shifts to lower energy as the oxidation state of the metal

increases. In other words, removing d-electrons results in less unpaired electrons, less excited state multiplets, and less ways for 3p-3d exchange coupling. For the redox couple $Fe^{2+}(d^6)/Fe^{3+}(d^5)$, this simple multiplet model does not suffice. Removing an electron from Fe^{2+} to create Fe^{3+} increases the number of unpaired electrons which pushes the $K\beta_{1,3}$ peak to the higher energy side. Removing an electron from Fe^{2+} , however, lessens the number of ways of creating excited states with the ligands, the effect being known in the literature as configuration interaction driven by covalency. Configuration interaction pushes the Fe^{3+} $K\beta_{1,3}$ peak to lower energy compared to Fe^{2+} . The result is that the resolution between the $K\beta$ XES features of Fe^{2+} and Fe^{3+} is not easy to detect.

These limitations of XES studies of Fe²⁺/Fe³⁺ are, however, on individual Fe2+ and Fe3+ systems. The crystalline environment of Fe₃O₄ is different. In the Fe₃O₄ crystal system, the competing influence of spin vs covalency should not be so severe as to wash out the resolution because, in Fe₃O₄ system, the Fe centers are always coordinated by only oxide ligands, and the geometry is constrained by the lattice; thus, there's less room for geometric changes that could complicate the analysis. We thus expect to see resolvable resolution in our studies. Specifically, in Fe₃O₄, half of the Fe³⁺ cations fill the smaller tetrahedral 8a sites, and the second half of the Fe³⁺ cations and the Fe²⁺ cations occupy the larger 16d octahedral sites. As shown in eq 2, the incorporation of one Li⁺ ion removes the tetrahedral Fe³⁺ to octahedral positions resulting in both Fe³⁺ and Fe²⁺ being in the same ligand environment. Fe3+ and Fe2+, being in different spin configuration but the same ligand environment, should demonstrate the effect of spin only, and as such, we should be able to see systematic changes in XES feature as the anode undergoes systematic discharging and recharging.

The XES spectra from the Fe₃O₄ NP anodes are shown in Figure 5, and we see no such effects in the XES scans from the samples. The XES results correlate with the XRD and Raman analysis dictating that the model proposed by eq 2 is not valid for SIBs. A further higher-resolution investigation was carried out on samples A–H (Figure S2) to determine possible small changes in the Fe₃O₄ crystal as a result of sodiation. In the highenergy resolution fluorescence detected (HERFD) X-ray studies, one scans through the X-ray absorption energy and detects at a single emission energy. By combining XES with X-ray absorption spectroscopy (XAS) in a resonant measurement, one can further enhance the selectivity. HERFD scan results are

shown in Figure 5c. Again, no distinction is seen even in these scans, pointing to our initial assumption that Na^+ ions are not inserted into the Fe₃O₄ structure.

Structural Relaxation Calculations of Na, Fe₃O₄, and Na_xFe₃O₄. DFT calculations were performed using Quantum Espresso software to study the structural relaxations (including lattice vectors) of Fe₃O₄, body centered cubic (bcc) Na, and Na_xFe₃O₄ using the Perdew–Burke–Ernzerhof (PBE) approximations. Following eq 2, one Na atom is inserted into the 16c Wyckoff position of the 14-atom Fe₃O₄ inverse spinel unit cell, as shown in Figure S1b. The voltage for the intercalation of a Na⁺ ion into Fe₃O₄ is found as the difference in total energies of the different constituents as³²

$$V = \left(\frac{E_{\text{intercalated}} - E_{\text{empty}} - E_{\text{metal}}}{n}\right) \tag{3}$$

Here, $E_{\rm intercalated}$ is the energy of the intercalated anode (e.g., Na_xFe₃O₄); $E_{\rm empty}$ is the energy of the empty anode (e.g., Fe₃O₄); $E_{\rm metal}$ is the energy per atom of a pure metal anode; and n is the valency of the intercalated cation. We note here that these calculations are based solely on the internal energy of each constituent. The more rigorous Gibbs free energy would require consideration of volume and entropic effects, but it has been shown to result in small corrections to internal energy while significantly increasing the computational time. ³²

Structural relaxations of Fe_3O_4 and $Na_xFe_3O_4$ (x=0.5) resulted in no discernible changes of the initial crystal structures. The volume of the unit cell, however, increased by 7% with x=0.5. Calculations of voltages using eq 3, however, resulted in negative voltage (V=-0.35 V vs Na/Na^+), meaning that sodiation of Fe_3O_4 in the form of $Na_xFe_3O_4$ (x=0.5) is unfavorable. Recent publications on DFT calculations of the intercalation of $Al_{0.20}$ in α - and ζ - V_2O_5 showed negative voltage values similar to ours: disadvantages of Al incorporation in the vanadium oxide cathode are well documented. $^{32-35}$ Hence, our DFT investigation points to the impracticality of the intercalation of Na^+ ions into Fe_3O_4 and further validates our experimental findings.

Surface Chemistry Analysis and Electrochemical **Diagnostics.** Having discussed the nonviability of Na⁺ ion insertion to conversion reactions in the Fe₃O₄ anode (eq 2) based on electrochemical analysis and advanced characterization results, we shift our attention to other possible mechanisms for the low capacity observed in our experiments and previous publications. SEM analysis and EDS elemental mapping were performed on the samples as functions of DoD and SoC to verify whether the origin of the capacity observed in Figure 2 could be Na⁺ adsorption/desorption onto the active electrode. As seen in the EDS plots and elemental mapping in Figures S6 and S7, Na is uniformly distributed in the discharged electrodes. Considering the ratio of the EDS intensities of Na to Fe a measure of the amount of Na⁺ ions adsorbed onto the electrodes, we plotted the ratio as functions of DoD and SoC in Figure 6a. While the analysis is qualitative, Figures S6 and S7 and Figure 6a do indicate that the Na+ ions are adsorbed on the electrodes progressively with increased DoD and desorbed from the electrodes gradually with increased SoC. We note here that six EDS elemental maps at each DoD and SoC were averaged to arrive at the plot of the ratios in Figure 6a. That this analysis is indeed qualitative is apparent in the last data point of Figure 6a that shows increased Na content in sample H compared to that in sample G.

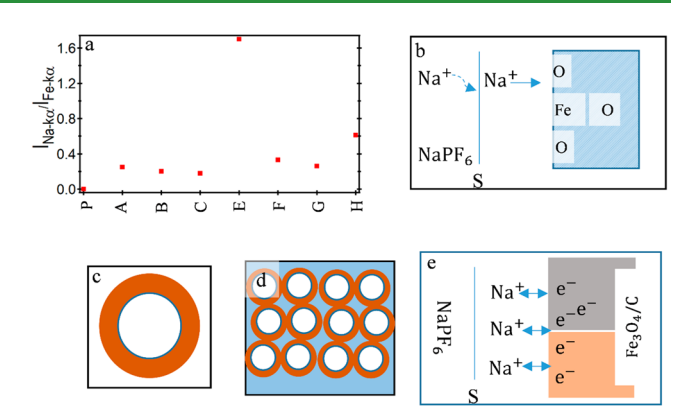


Figure 6. (a) The ratio of the EDS intensities of Na to Fe as functions of DoD and SoC qualitatively indicates that Na⁺ ions are adsorbed on the electrodes progressively with increased DoD and desorbed gradually with increased SoC. In panel a, the x-axis refers to the cycled electrodes A–H, with P being the pristine electrode. (b) Possible Na⁺ ion storage and conductivity enhancement in the Fe₃O₄ NP-based electrode could entail an attractive interaction between the Na+ ions in the electrolyte and the Fe₃O₄ NPs in the electrode that results in a narrow interfacial region devoid of Na+ ions immediately outside the interface. For oxide NPs in the electrolyte, a conformal space charge region (c, orange annulus) devoid of cations is created. (d) In an ensemble of NPs in the electrolyte, both cation storage and ionic conductivity are enhanced when the conformal space charge regions reach the percolation threshold. (e) Synergistic effects between an ion conducting interface and an electron conducting electrode may enhance the charge storage capacity of electrochemical cells.

In Figure 2, we observe 50 mA h/g of specific capacity for bulk Fe_3O_4 -based electrodes, which improves to around 100 mA h/g for Fe_3O_4 NP-based electrodes. Possible explanations for the observation could be as follows:

- (a) The 50 mA h/g capacity of bulk Fe_3O_4 and the 100 mA h/ g capacity of Fe₃O₄ NPs could result from the formation of a solid electrolyte interphase (SEI) on the electrode surface with possible side reactions (e.g., electrolyte decomposition). As shown in Figure 2d, the reversible capacities upon cycling may infer the efficiency of the conductive SEI layer for Na⁺ ion storage. In general, SEI formation on the anode side is considered a result of reductive decomposition of electrolyte. Therefore, discharge capacity is more related to SEI formation. As bulk Fe₃O₄ has a bigger crystallite size than synthesized NPs, its surface area is lower, and as such, the demonstrated initial lower discharge capacity of bulk Fe_3O_4 as compared to that of Fe_3O_4NPs points to the role played by the SEI in these half cells. Further study of the formed and evolved SEI layers could shed more light on
- (b) Surface ion storage (e.g., mostly adsorption and desorption) on NPs is a well-known phenomenon. TEM investigations show that most NPs are endowed with surface facets, since they are nanosize versions of the original crystal (Figure 1b). Many of these facets contain defects and can store free ions. As shown in the Supporting Information, the total surface area of particles is proportional to 1/r, with r being the radius of the particles. As such, it makes qualitative sense that the capacity of electrodes composed of NPs is larger than that with bulk Fe₃O₄. Quantitatively, using 100 mA h/g of capacity with 8.5 nm Fe₃O₄ NPs, we calculate a storage of

3736 Na⁺ ions on the surface of each Fe₃O₄ NP (see the Supporting Information). However, based on our previous work on Fe₃O₄ NPs, we deem this number of ions per NP to be unrealistic; we have demonstrated that individual NP facets are capable of storing at best one free ion.³⁶

To complement the trivial size effect, we turn to a nanostructuring induced enhancement of charge storage and ionic conductivity at the heterointerface between the Fe₃O₄ NPbased electrode and the NaPF₆-based electrolyte with dissimilar work function, a phenomenon formally known as *nanoionics*.

Nanoionics Effects. Nanoionics effects are the enhancement of ionic conductivity and ionic storage at heterogeneous interfaces, such as between a metal and a semiconductor, between an electrolyte and an oxide (e.g., LiI-Al₂O₃ system), or, as in our case, between the NaPF₆-based electrolyte and the Fe₃O₄ NP-based electrode. Nanoionics phenomena are qualitatively similar to Schottky barriers that result in local migration of mobile ions within a heterogeneous interphase due to the difference in work functions of the two materials.^{37–39} A space charge layer formed at such interphases can contribute to enhanced ionic and electronic conductivity, and improved charge transfer reaction kinetics. Such effects have already been observed in LIBs with RuO₂ electrodes that form the Li₂O/Ru composite upon reduction. TRu does not allow Li⁺ ions in its crystal structure but is a good electronic conductor. On the contrary, Li₂O does admit Li⁺ ions but is a poor electronic conductor. A compensatory and synergistic effect develops at the interfacial region of the Li₂O/Ru composite where up to a monolayer storage of Li+ ions takes places leading to high capacity and reversibility of the battery.

Two types of nanoionics interactions between a Frenkel disordered crystal M+X- (e.g., AgCl and NaPF₆) and a chemically inert material A (e.g., Al₂O₃ and Fe₃O₄) are possible.^{37–39} The first is surface stabilization of M⁺ ions by A, where the M⁺ cations are attracted to the interface that lowers the free energy of vacancy formation and enlarges the free energy of interstitial formation compared to the intrinsic values. This creates a layer of M⁺ ion vacancies at the interface. In the second scenario where a repulsive interaction between A and interfacial M⁺ is more energetically favorable, the latter are driven into the interstitial sites of M⁺X⁻. The end results are the same for both cases: an interfacial region of M⁺ ion vacancies and possibility of extrinsic conductivity enhancement at the interface. As a specific example of nanoionics at the heterogeneous interface, Maier et al. considered the addition of fine-grained insulating Al_2O_3 particles to $AgCl.^{40-42}$ The defect concentration in AgCl is small, but cation mobility is significant. As the basic oxide Al₂O₃ adsorbs the mobile Ag+ cations, excess cation vacancies are formed in the AgCl matrix adjacent to the Al₂O₃. This composite system can now act as a high mobility conduit with a high concentration of cation vacancies. We hypothesize that a similar interaction between the NaPF₆-based electrolyte and the Fe₃O₄ NP-based electrode occurs in our electrochemical cells, as shown schematically in Figure 6b.

Quantitative analysis of such a system can be performed by realizing that such an effect is related to the standard free enthalpy and mass action constant, and relating the local cation concentration to the standard free enthalpy. 40-42 Similar to the p-n junctions, the concentration profile can be obtained from Poisson's equation with imposition of constant electrochemical potential and the boundary condition that the electric field $(-\partial \varphi/\partial x)$ vanishes in the interior. The concentration profile is found to be functions of the Gibbs free energy for vacancy (or interstitial) formation, Debye length, and temperature:

$$C_{v}(x) = C_{v}(0) f(x, \Delta_{v} G^{\circ}, \lambda, T)$$
(4)

Here, $C_v(0)$ is the concentration at the interface (x = 0), x is the position measured from the interface and going inward into M^+X^- , $\Delta_v G^0$ is the Gibbs free energy of vacancy formation in $\mathrm{M}^{+}\mathrm{X}^{-}$, λ is the Debye length, and T is the temperature. The Debye length (λ) determines the fall of the interfacial charge distribution into the interior and is given by

$$\lambda = \left(\frac{\in \in_{0kT}}{2e^2 c_{\infty}}\right)^{1/2} \tag{5}$$

Here, ϵ is the permittivity of M⁺X⁻, ϵ_0 is the vacuum permittivity, and c_{∞} is the concentration in bulk M⁺X⁻.

Assuming an attractive interaction between Na⁺ ions and Fe₃O₄ (6b) in our electrochemical cells, a conformal space charge region devoid of cations is created (Figure 6c, orange annulus) that can store high-density Na+ ions. In addition to enhanced cation storage, cation conductivity can also drastically improve at the space charge region (λ). The global conductivity is influenced by the so-called parallel switching that takes into account the connectivity of the space charge layers (Figure 6d), similar to the percolation scenario. Rigorous calculations for the M⁺X⁻/A system by Maier et al. show that the total conductance is given by

$$\sigma_{\rm m} = (1 - \varphi_{\rm A})\sigma_{\infty} + (3\sqrt{2})\beta_{\rm L}(\varphi_{\rm A}/r_{\rm A})\sqrt{\in \in_0 RT/V^{\rm m}}u_{\rm V}(N_{\rm V0})^{1/2}$$
(6)

Here, φ_A is the volume fraction of the inert phase A; σ_{∞} is the conductance of the M^+X^- system; β_L takes into account the parallel switching correction; r_A is the mean radius of the A particles; V^{m} is the molar volume; u_{V} is the mobility of vacancies; and N_{V0} is the vacancy concentration at the interface. The quantitative concentration profile $C_{\nu}(x)$, Debye length λ , and conductivity enhancement $\sigma_{\rm m}$ can be determined if the relevant Gibb's free energy, surface concentration, and mobilities are known. This has been done for the AgCl:Al₂O₃ and AgCl:SiO₂ systems. 40-42

We suggest that similar nanoionics effects take place in our NaPF₆-based electrolyte:Fe₃O₄ NP-based electrode system. We are, however, not able to provide a quantitative answer for the concentration profile, because the relevant Gibbs free energy, surface concentration, and mobilities are not known. We suggest that the capacity seen in our electrochemical cells and capacity enhancement with a nanostructured electrode is due to enhancement of Na+ ion storage and conductivity at the interphase in the system based on the following: (1) Fe₃O₄ is a ceramic with the highest known conductivity; DFT calculations indicate Fe₃O₄ to be without a band gap at the Fermi level. (2) The carbon we used in the slurry is also conducting, so it seems that the slurry is an electrical conductor. (3) Our exhaustive experimental and theoretical studies have shown that Fe₃O₄ is not a Na⁺ ion conductor. Following the nanoionics phenomenon, therefore, we hypothesize that a space charge region develop at the interfacial region between the Fe₃O₄ NP-based electrode and the NaPF₆-based electrolyte that becomes a storage and a conduit for Na⁺ ion conduction (Figure 6e).

Simple calculations (Figure S5) based on close packing of 50 nm diameter bulk Fe₃O₄ and 8.5 nm diameter Fe₃O₄ NPs show that the space charge layer length is inversely proportional to the square of the particle diameter, $1/r^2$. The capacity further depends on the conductivity of the space charge layer, given above by eq 6. Many terms on the conductivity equation are sample-specific, and we do not have definite numerical values for our Fe₃O₄/NaPF₆ system; thus, we attempt to make some simple assumptions. The first term in eq 6 is the conductivity of pure NaPF₆-based electrolyte, and it is the same for both bulk Fe₃O₄- and Fe₃O₄ NP-based electrodes. The value of β_L is used as a number close to unity for parallel switching, so we may assume it to be the same for both systems. Also, the volume fraction of Fe₃O₄ (φ _A) is the same (70%) for both systems. The terms under the square root sign are the internal properties of Fe₃O₄, and they are also the same for both systems. Finally, the mobility of vacancies (u_v) and vacancy concentration at the interface (N_{V0}) refer to the NaPF₆-based electrolyte, and it is reasonable to assume these values to remain the same when we change over from bulk Fe₃O₄ to Fe₃O₄ NPs. It seems that the only factor influencing the conductivity enhancement is the inverse of the particle radius, 1/r.

Combining the effects of surface charge storage (1/r), nanoionics-induced space charge layer length $(1/r^2)$, and the conductivity enhancements (1/r), we can qualitatively see that the capacity in the electrodes composed of NPs should be significantly larger than those made with bulk Fe₃O₄. In practice, however, we see a capacity enhancement by a factor of only 2 for the Fe₃O₄ NP-based system. A possible explanation for the discrepancy is that only the nanosizing effect cannot provide a comprehensive understanding of the nanostructuring phenomenon. Small nanoparticles have an overwhelming percentage of atoms on their surfaces with a number of dangling bonds, which result in detrimental effects—unwanted side reactions including electrolyte decomposition—on battery performance. We believe that such effects may lower the capacity of the cells with NP anodes.

The final point that needs to be addressed is that the 100 mA h/g capacity of the Fe₃O₄ NP-based electrode still corresponds to on the order of 3736 Na⁺ capacity per NP, as described earlier. We believe that the difference between our calculation (see Supporting Information) and the limited storage ability of NP facets not being able to store more than one free charge and additional storage induced by nanoionics is related to a dynamic effect. As shown in Figure 6e, this dynamic capacity could entail a capacitive effect between the Na⁺ ions in the space charge region and the electrons in the Fe₃O₄ NP-based electrode.

SUMMARY AND CONCLUSIONS

The concept of the SIB as a viable alternative to LIBs deserves serious effort because sodium is an element that is indeed in unlimited supply on the earth. At the same time, the concept of IS-TMO, especially Fe_3O_4 , as a conversion-type electrode for SIB is worthy of investigation. Just like sodium, iron oxides are easily sourceable, are stable in the ambient, contribute to a minimal environmental footprint, and are easily recyclable. Our efforts, however, demonstrate that the widely accepted notion of using a knowledge base for LIBs in the construction of SIBs has limited reach. Specifically, a combination of electrochemical analysis and diagnostics, X-ray-based and spectroscopic analysis, and first principle modeling shows that Thackeray et al.'s model that has been used successfully to demonstrate the intercalation to conversion of Fe₃O₄ as anodes for LIBs is unworkable for SIBs. We instead propose a model of sodiation electrochemistry in Fe₃O₄ in terms of the creation of a space charge channel

between the Fe₃O₄ NP-based electrode and the NaPF₆-based electrolyte.

ASSOCIATED CONTENT

Supporting Information

The Supporting Information is available free of charge at https://pubs.acs.org/doi/10.1021/acsami.2c13016.

Crystal structures, DoD and SoC sample descriptions, Liion half-cell description, dQ/dV plots, nanoparticle surface chemistry calculations, and EDS elemental mapping plots (PDF)

AUTHOR INFORMATION

Corresponding Authors

Mohammad A. Islam – Department of Physics, State University of New York at Oswego, Oswego, New York 13126, United States; orcid.org/0000-0002-8617-4858; Email: mohammad.islam@oswego.edu

Sang-Don Han – Materials, Chemical, and Computational Science Directorate, National Renewable Energy Laboratory, Golden, Colorado 80007, United States; o orcid.org/0000-0002-2931-659X; Email: sang-don.han@nrel.gov

Authors

Jared Bouldin – Department of Physics, State University of New York at Oswego, Oswego, New York 13126, United States Junghoon Yang – Carbon Materials Application Research Group, Korea Institute of Industrial Technology, Jeonju-si, Jeollabuk-do 54853, Republic of Korea

Complete contact information is available at: https://pubs.acs.org/10.1021/acsami.2c13016

Notes

The authors declare no competing financial interest.

ACKNOWLEDGMENTS

This work was authored in part by Alliance for Sustainable Energy, LLC, the manager and operator of the National Renewable Energy Laboratory (NREL) for the U.S. Department of Energy (DOE) under Contract DE-AC36-08GO28308. Funding for material synthesis and electrochemical characterization was provided by the Laboratory Directed Research and Development program. This work was supported in part by the U.S. Department of Energy, Office of Science, Office of Workforce Development for Teachers and Scientists (WDTS) under the Visiting Faculty Program (VFP). This material is based upon work supported by the National Science Foundation Platform for the Accelerated Realization, Analysis, and Discovery of Interface Materials (PARADIM) under Cooperative Agreement DMR-2039380. The views expressed in the article do not necessarily represent the views of the DOE or the U.S. Government.

REFERENCES

- (1) Chayambuka, K.; Mulder, G.; Danilov, D. L.; Notten, P. H. Sodium-Ion Battery Materials and Electrochemical Properties Reviewed. Adv. Energy Mater. 2018, 8, 1800079.
- (2) Liang, Y.; Lai, W.-H.; Miao, Z.; Chou, S.-L. Nanocomposite Materials for the Sodium-Ion Battery: A Review. Small 2018, 14, 1702514.
- (3) Yang, C.; Xin, S.; Mai, L.; You, Y. Materials Design for High-Safety Sodium-Ion Battery. Adv. Energy Mater. 2021, 11, 2000974.

- (4) Xiao, B.; Rojo, T.; Li, X. Hard Carbon as Sodium-Ion Battery Anodes: Progress and Challenges. *ChemSusChem* **2019**, *12*, 133–144.
- (5) Ha, D.-H.; Islam, M. A.; Robinson, R. D. Binder-Free and Carbon-Free Nanoparticle Batteries: A Method for Nanoparticle Electrodes without Polymeric Binders or Carbon Black. *Nano Lett.* **2012**, *12*, 5122–5130.
- (6) Islam, M. A.; Zuba, M.; DeBiase, V.; Noviasky, N.; Hawley, C. J. High Capacity Lithium Ion Batteries Composed of Cobalt Oxide Nanoparticle Anodes and Raman Spectroscopic Analysis of Nanoparticle Strain Dynamics in Batteries. *Nanotechnology* **2018**, *29*, 075403.
- (7) Cabana, J.; Monconduit, L.; Larcher, D.; Palacín, M. R. Beyond Intercalation-Based Li-Ion Batteries: The State of the Art and Challenges of Electrode Materials Reacting Through Conversion Reactions. *Adv. Mater.* **2010**, *22*, E170–E192.
- (8) Goodenough, J. B.; Kim, Y. Challenges for Rechargeable Li Batteries. *Chem. Mater.* **2010**, 22, 587–603.
- (9) Komaba, S.; Mikumo, T.; Yabuuchi, N.; Ogata, A.; Yoshida, H.; Yamada, Y. Electrochemical Insertion of Li and Na Ions into Nanocrystalline Fe₃O₄ and α -Fe₂O₃ for Rechargeable Batteries. *J. Electrochem. Soc.* **2010**, *157*, A60–A65.
- (10) Valvo, M.; Lindgren, F.; Lafont, U.; Björefors, F.; Edström, K. Towards More Sustainable Negative Electrodes in Na-ion Batteries via Nanostructured Iron Oxide. *J. Power Sources* **2014**, *245*, 967–978.
- (11) Hariharan, S.; Saravanan, K.; Ramar, V.; Balaya, P. A Rationally Designed Dual Role Anode Material for Lithium-ion and Sodium-ion Batteries: Case Study of Eco-friendly Fe₃O₄. *Phys. Chem. Chem. Phys.* **2013**, *15*, 2945–2953.
- (12) Thackeray, M. M.; David, W. I. F.; Goodenough, J. B. Structural Characterization of the Lithiated Iron Oxides $\text{Li}_x\text{Fe}_3\text{O}_4$ and $\text{Li}_x\text{Fe}_2\text{O}_3$ (0 < x < 2). *Mater. Res. Bull.* **1982**, *17*, 785–793.
- (13) Zhang, W.; Bock, D. C.; Pelliccione, C. J.; Li, Y.; Wu, L.; Zhu, Y.; Marschilok, A. C.; Takeuchi, E. S.; Takeuchi, K. J.; Wang, F. Insights into Ionic Transport and Structural Changes in Magnetite during Multiple-Electron Transfer Reactions. *Adv. Energy Mater.* **2016**, *6*, 1502471.
- (14) He, K.; Zhang, S.; Li, J.; Yu, X.; Meng, Q.; Zhu, Y.; Hu, E.; Sun, K.; Yun, H.; Yang, X.-Q.; Zhu, Y.; Gan, H.; Mo, Y.; Stach, E. A.; Murray, C. B.; Su, D. Visualizing Non-equilibrium Lithiation of Spinel Oxide via *in situ* Transmission Electron Microscopy. *Nat. Commun.* **2016**, *7*, 11441.
- (15) Taberna, P. L.; Mitra, S.; Poizot, P.; Simon, P.; Tarascon, J.-M. High Rate Capabilities Fe_3O_4 -based Cu Nano-architectured Electrodes for Lithium-ion Battery Applications. *Nat. Mater.* **2006**, *5*, 567–573.
- (16) Chevrier, V. L.; Ceder, G. Challenges for Na-ion Negative Electrodes. *J. Electrochem. Soc.* **2011**, *158*, A1011–A1014.
- (17) Lee, J.; Zhang, S.; Sun, S. High-Temperature Solution-Phase Syntheses of Metal-Oxide Nanocrystals,. *Chem. Mater.* **2013**, 25, 1293—1304.
- (18) Hou, B.; Wan, Y.; Guo, J.; Zhang, Y.; Ning, Q.; Yang, Y.; Li, W.; Zhang, J.; Wang, X.; Wu, X. A Scalable Strategy To Develop Advanced Anode for Sodium-Ion Batteries: Commercial Fe₃O₄-Derived Fe₃O₄@ FeS with Superior Full-Cell Performance. *ACS Appl. Mater. Interfaces* **2018**, *10*, 3581–3589.
- (19) Liu, H.; Jia, M.; Zhu, Q.; Cao, B.; Chen, R.; Wang, Y.; Wu, F.; Xu, B. 3D-0D Graphene-Fe₃O₄ Quantum Dot Hybrids as High-Performance Anode Materials for Sodium-Ion Batteries. *ACS Appl. Mater. Interfaces* **2016**, *8*, 26878–26885.
- (20) Xu, J.; Zhang, X.; Miao, Y.; Wen, M.; Yan, W.; Lv, P.; Wang, J.; Sun, Q. In-situ plantation of Fe3O4@C nanoparticles on reduced graphene oxide nanosheet as high-performance anode for lithium/sodium-ion batteries. *Appl. Surf. Sc* 2021, 546, 149163.
- (21) Wang, Q.; Ma, Y.; Liu, L.; Yao, S.; Wu, W.; Wang, Z.; Lv, P.; Zheng, J.; Yu, K.; Wei, W.; Ostrikov, K. Plasma Enabled Fe₂O₃/Fe₃O₄ Nano-aggregates Anchored on Nitrogen-doped Graphene as Anode for Sodium-Ion Batteries. *Nanomaterials* **2020**, *10*, 782.
- (22) Tao, X.; Li, Y.; Wang, H.; Lv, X.; Li, Y.; Xu, D.; Jiang, Y.; Meng, Y. Multi-heteroatom-doped dual carbon-confined Fe_3O_4 nanospheres as high-capacity and long-life anode materials for lithium/sodium ion batteries. *J. Colloid Interface Sc* **2020**, *565*, 494–502.

- (23) Li, J.; Qin, W.; Xie, J.; Lin, R.; Wang, Z.; Pan, L.; Mai, W. Rational design of MoS₂-reduced graphene oxide sponges as free-standing anodes for sodium-ion batteries. *Chem. Eng. J.* **2018**, 332, 260–266.
- (24) Li, J.; Ding, Z.; Li, J.; Wang, C.; Pan, L.; Wang, G. Synergistic coupling of NiS_{1.03} nanoparticle with S-doped reduced graphene oxide for enhanced lithium and sodium storage. *Chem. Eng. J.* **2021**, 407, 127199
- (25) Li, J.; Ding, Z.; Pan, L.; Li, J.; Wang, C.; Wang, G. Facile self-templating synthesis of layered carbon with N, S dual doping for highly efficient sodium storage. *Carbon* **2021**, *173*, 31–40.
- (26) Zhang, Y.; Li, J.; Ma, L.; Li, H.; Xu, X.; Liu, X.; Lu, T.; Pan, L. Insights into the storage mechanism of 3D nanoflower-like V_3S_4 anode in sodium-ion batteries. *Chem. Eng. J.* **2022**, 427, 130936.
- (27) Shebanova, O. N.; Lazor, P. Raman Spectroscopic Study of Magnetite (FeFe₂O₄): A New Assignment for the Vibrational Spectrum. *J. Solid State Chem.* **2003**, *174*, 424–430.
- (28) Panta, P. C.; Bergmann, C. P. Raman Spectroscopy of Iron Oxide of Nanoparticles (Fe₃O₄). *J. Material Sci. Eng.* **2015**, *5*, 1000217.
- (29) Gamblin, S. D.; Urch, D. S. Metal $K\beta$ X-ray Emission Spectra of First Row Transition Metal Compounds. *J. Electron Spectrosc. Relat. Phenom.* **2001**, *113*, 179–192.
- (30) Kowalska, J. K.; Lima, F. A.; Pollock, C. J.; Rees, J. A.; DeBeer, S. A Practical Guide to High-resolution X-ray Spectroscopic Measurements and Their Applications in Bioinorganic Chemistry. *Isr. J. Chem.* **2016**, *56*, 803–815.
- (31) Yamaoka, H.; Oura, M.; Taguchi, M.; Morikawa, T.; Takahiro, K.; Terai, A. $K\beta$ Resonant X-ray Emission Spectroscopy for Fe, Fe₂O₃ and Fe₃O₄. *J. Phys. Soc. Jpn.* **2004**, *73*, 3182–3191.
- (32) Shepard, R.; Smeu, M. Ab initio Investigation of α and ζ -V₂O₅ for Beyond Lithium Ion Battery Cathodes. J. Power Sources **2020**, 472, 228096.
- (33) Meng, Y. S.; Arroyo-de Dompablo, M. E. First Principles Computational Materials Design for Energy Storage Materials in Lithium Ion Batteries. *Energy Environ. Sci.* **2009**, *2*, 589–609.
- (34) Kulish, V. V.; Manzhos, S. Comparison of Li, Na, Mg and Al-ion Insertion in Vanadium Pentoxides and Vanadium Dioxides. *RSC Adv.* **2017**, *7*, 18643–18649.
- (35) Rong, Z.; Malik, R.; Canepa, P.; Sai Gautam, G.; Liu, M.; Jain, A.; Persson, K.; Ceder, G. Materials Design Rules for Multivalent Ion Mobility in Intercalation Structures. *Chem. Mater.* **2015**, *27*, 6016–6021.
- (36) Islam, M. A.; Xia, S. Electrostatic Properties of Maghemite (γ-Fe₂O₃) Nanocrystalline Quantum Dots Determined by Electrophoretic Deposition. *J. Phys.: Condens. Matter* **2009**, *21*, 285301.
- (37) Maier, J. Space Charge Regions in Solid Two-phase Systems and Their Conduction Contribution—I. Conductance Enhancement in the System Ionic Conductor-'Inert' Phase and Application on AgC1:Al₂O₃ and AgC1:SiO₂. J. Phys. Chem. Solids 1985, 46, 309–320.
- (38) Balaya, P.; Li, H.; Kienle, L.; Maier, J. Fully Reversible Homogeneous and Heterogeneous Li Storage in RuO₂ with High Capacity. *Adv. Funct. Mater.* **2003**, *13*, 621–625.
- (39) Maier, J. Nanoionics: Ion Transport and Electrochemical Storage in Confined Systems. *Nat. Mater.* **2005**, *4*, 805–815.
- (40) Maier, J. Ionic Conduction in Space Charge Regions. *Prog. Solid State Chem.* **1995**, 23, 171–263.
- (41) Maier, J. Kröger-vink Diagrams for Boundary Regions. *Solid State Ion* **1989**, 32-33, 727–733.
- (42) Maier, J. Nanoionics: Ionic Charge Carriers in Small Systems. *Phys. Chem. Chem. Phys.* **2009**, *11*, 3011–3022.